Original Paper

Shale gas transport in nanopores with mobile water films and water bridge

Ran Li [a], Zhangxin Chen [a, b, *], Keliu Wu [a, b], Jinze Xu [a]

[a] Department of Chemical and Petroleum Engineering, University of Calgary, Calgary, Alberta, T2N 1N4, Canada
[b] State Key Laboratory of Petroleum Resources and Prospecting, China University of Petroleum (Beijing), Beijing, 102249, China

ABSTRACT

Gas flow properties in nanopores are significantly determined by the flow patterns. Slug flow pattern is a potential water–gas two phase flow pattern, in which gas molecules flow in form of gas slugs and water molecules separate gas slugs. Considering water slippage, a portion of water molecules accumulates at the wall with lower mobility, while the remaining water molecules take the shape of a water bridge. Adopting foam apparent viscosity model to represent slug rheological behavior, how water bridge disturbs on gas flow capacity is estimated. The results are compared with the water–gas two phase flow model that assumes annular flow pattern as well as the single gas flow model without the consideration of water. The comparison illustrates that gas molecular movement is significantly hindered by flow space reduction and loss of gas slippage. The impact from water phase of slug flow pattern is more significant than that of annular flow pattern on gas flow capacity. It is discovered that larger nanopores improve gas flow capacity while maintaining bulk water layer thickness and increasing water bridge thickness tend to reduce gas transport ability. A better understanding of the structure and transport of water and gas molecules is conducive to figure out the specific gas–water flow behavior and predict shale gas production.

1. Introduction

Shale gas is achieving a prominent position in the global market due to energy demand and technology developments. To perform accurate reserve evaluation and improve gas recovery efficiency, there is a need to clarify fluid flow patterns and transport mechanisms in the complicated shale rocks containing multiscale fractures and pores such as artificial fractures, natural fractures, micropores and nanopores (Garum et al., 2019; Jia et al., 2020; Mistré et al., 2018; Wang et al., 2020; Xu et al., 2017, 2018a; Rubin et al., 2019).

Gas–water multiphase flow in nanoscale pores has been investigated by various experiments, simulations and analytical models, which is quite different from the two-phase flow in conventional reservoirs. Firstly, the molecular interactions between liquid molecules and solid molecules of pore surface should be considered as they are drastic enough to be comparable with liquid–liquid molecular interactions in the nanoscale pores. Nanopore properties such as chemical composition (Cristancho-Albarracin et al., 2017; Kibria et al., 2018; Yassin et al., 2017), pore shape (Sun et al., 2019; Xu et al., 2019b; Song et al., 2020a), pore size (Hatami et al., 2020; Ho and Wang, 2020; Xu et al., 2018b, 2019a; Yin et al., 2017), surface roughness (Hou et al., 2020; Tesson and Firoozabadi, 2018; Zeng et al., 2018), liquid properties such as liquid type (Wang et al., 2019; Wan and Mu, 2018; Zuo et al., 2018), and viscosity and solid–liquid molecular collisions (Alharthy et al., 2016; Song et al., 2020b; Xiong et al., 2017) in different reservoir conditions (Gupta et al., 2018; Herdes et al., 2018; Islam and Sun, 2017; Jin and Firoozabadi, 2015; Swami et al., 2012; Wang et al., 2018) are analyzed to calculate how liquid spreads at the solid surface. Also, connate water and fracturing liquid enables the co-existence of water and gas molecules in nanoscale shale channels. The existence of water molecules occupies gas flow area and disturbs gas flow pattern, resulting in a gas–water two phase flow deviating significantly from the single-phase flow (Guo et al., 2019; Li et al., 2017; Xu et al., 2020). Understanding the structure and transport of water molecules is crucial to figure out the specific gas–water relative permeability curves in the corresponding

---

nanopores and conduct accurate shale gas reserve evaluation. Therefore, it is necessary to determine the water−gas flow patterns to obtain gas−water flow capacity. As typically observed fluid flow pattern in nanoscale pores, annular flow pattern and slug flow pattern are used to calculate shale gas transport in nanopores with mobile water films and water bridge. Li et al. (2019) predicted water−gas flow behavior with annular flow pattern, and this study uses slug flow pattern to calculate water−gas transport capacity. The results are compared to evaluate the impact of structure and transport of water molecules on gas flow in shale nanopores.

Annular flow pattern is frequently observed in nanoscale pores both in molecular dynamic (MD) simulations and laboratory experiments. In annular flow, water molecules transport in form of water film at the wall of nanopores, while gas molecules flow in the central area. Liu et al. (2018) placed 2100 water molecules and 700 methane molecules into a slit model measuring 5.012 nm × 7.16 nm × 10 nm to explore how methane and water distributed in hydrophilic nanoscale space under different reservoir conditions. A group of almost sticking water molecules were found to move along the substrate with an extra low velocity, while the other group of water molecules travelled at a larger speed. The reason accounting for the property difference was attributed to the hydrogen bond created between near-surface water molecules and solid molecules. In the meantime, gas molecules mainly passed the channel though the central area. Applying a larger driving pressure difference was likely to improve the velocity difference between water phase and gas phase. Likewise, Ho and Striolo (2015) used 1800 water molecules and 600 methane molecules to observe two phase flow with a 2.65−5.00-nm-sized shale simulation model at 75 and 250 MPa. An analogous annular flow pattern at certain accelerations had been detected. Besides, Wu et al. (2013) observed gas−water flow directly with visual displacement experiments in 1D nano-range channels. Optic images were captured with epi-fluorescence microscopy to discover the specific flow behavior in which gas molecules aggregated in the center and surrounded with a water film measuring 0.9−1.6 nm at the wall. Based on the observed phenomenon, a variety of analytical models considering annular gas−water two phase flow have been put forward to better predict shale gas flow capacity in a wet condition. Li et al. (2016a) analyzed the impacts of water film on gas adsorption by calculating intermolecular forces between static water molecules and solid surface. Sun et al. (2017) declared that the spread of water molecules between gas and pore surface tended to reduce gas transport capacity by 11%.

Besides the annular flow pattern, slug flow pattern is also captured at different reservoir conditions. In slug flow, gas molecules flow in form of gas slugs and water molecules separate those gas slugs in form of liquid slugs. However, unlike the water film structure, there are only a little literature describing and analyzing the nanoscale water−gas bubble flow. Wu et al. (2013) employed epi-fluorescence microscopy combined with nanofluidic chips approach and discovered a flow type in which gas occupied in the majority of the 100-nm-deep slit-like nanochannel with discrete water slugs existing in between. Ho and Striolo (2015) studied the water bridge and they concluded similarly that water bridge would collapse and turned into water layers once a larger acceleration was applied. Liu et al. (2018) declared that the structure of gas bubble separated by water bridge were discovered when the pressure difference was small in the high-pressure condition (60−90 MPa). However, the water bridge would be destroyed at a larger pressure difference when the gas phase broke through. At this time, the water bridge thickness became smaller and smaller as water molecules left the water bridge and turned into the form of water film. Unlike Wu et al. (2013), Ho and Striolo (2015) and Liu et al. (2018), who investigated water structures during the pressure-driven flow,

Li et al. (2017) described the change of water structure with relative humidity. They claimed that the adsorbed water film initiates to become thicker and thicker with the increase of water vapor pressure. Once the critical relative humidity was achieved, the film became unstable and the water bridge was formed. The desorption of water molecules from the bridge also happened when the relative humidity was reduced.

The mentioned studies mainly focus on the observation of water bridge structures with MD simulation and displacement experiments, yet there are few analytical models proposed to describe the gas−water two phase slug flow pattern qualitatively and quantitatively in shale nanopores. Consequently, an analytical model is put forward to estimate how a mobile low-mobility water layer and a water bridge with bulk water properties exert influences on gas flow behavior in nanopores, which is further compared with previously derived annular flow model to reveal the importance of water structure. Also, the influencing factors such as pore dimension, water content and applied pressure are assessed to evaluate their significance. Different from previous studies which assumes annular water−gas two phase flow, this study puts forward the potential slug water−gas two-phase flow pattern, which is conducive to a more comprehensive understanding of fluid flow and production prediction in share reservoirs.

2. Model establishment

The model in this study is shown in Fig. 1. Fig. 1a shows the three dimensions of the nanoscale model. Gas and water flow along the x axis, and the thickness of the slit pore is h. For most previous studies and the analytical model that is used to be compared in this study, annular flow is assumed as in Fig. 1d. There are three divided flow regions for an ideal annular flow type (Fig. 1d), in which are a near-surface water film composed of low-mobility water molecules as a result of solid molecular attractions, a gas flow zone at the central area and a water layer made up of bulk water molecules staying in between. In contrast, in terms of slug flow, a proportion of bulk water molecules accumulate in form of water bridge at the pore center while the low-mobility water molecules and the remaining bulk water molecules still stay at the solid surface in form of two distinct water films with uniform thickness. Fig. 1b describes an extreme situation when all bulk water molecules are reserved in form of water bridge, serving as a liquid slug to block the advancement of gas molecules. Fig. 1c shows the other extreme situation in which the thickness of water bridge approaches the critical thickness and all the other bulk water molecules spread uniformly along the wall. The potential slug flow takes any flow pattern between these two extreme conditions. In this way, two extreme impacts of slug flow on shale gas are evaluated and compared with the annular flow condition.

It is assumed that all water molecules other than those that are between gas slugs are distributed as uniform water film along the pore wall. The pore wall is assumed to be smooth and flat. Besides, the water phase contains only pure water. Phase transformation between water and gas is not considered in the model.

2.1. Water bridge

The structure of methane bubble wrapped in water bridge resembles the foam flow in the porous media. Consequently, the analytical model to calculate foam properties is introduced to predict the fluid flow characteristics of the foam zone.

As is known, foam has a complicated structure containing water phase and gas phase. Due to the specified composition, gas relative permeability is reduced by slow bubbles. Meanwhile, water film impedes gas movement and therefore generates an enhanced gas
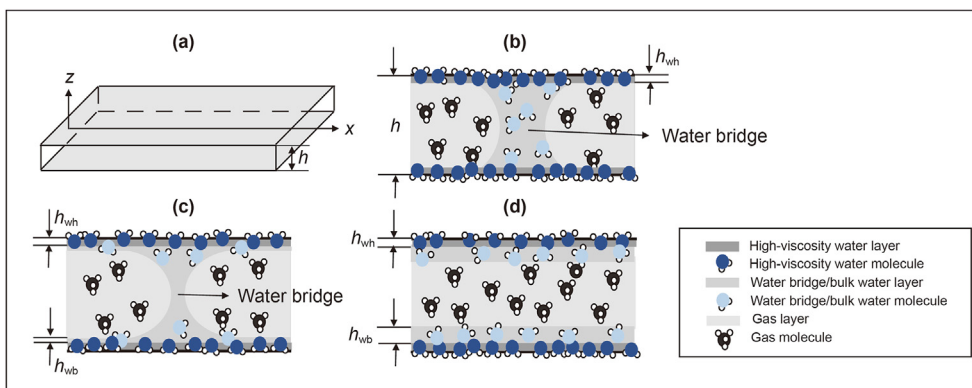
Fig. 1. (**a**) 3 dimensions of the model; (**b**) Distribution pattern of water−gas molecules (slug flow model when all bulk water molecules are reserved in form of water bridge); (**c**) Distribution pattern of water−gas molecules (slug flow model when the thickness of water bridge approaches the critical thickness and all the other bulk water molecules spread uniformly along the wall); (**d**) Distribution pattern of water−gas molecules (annular flow model).

apparent viscosity. Previous research demonstrates that it is difficult to distinguish individual impacts of bubbles on gas relative permeability and viscosity. It is a common approach to select the modification of gas relative permeability or gas viscosity to represent the overall change of gas mobility (Alcorn et al., 2020; Fu and Liu, 2020; Yekeen et al., 2018). A mathematical model predicting foam apparent viscosity in smooth capillaries is used to evaluate the influences of water bridge on gas flow in nanopore. Hirasaki and Lawson (1985) developed an analytical model (Eq. (1)) to obtain bubble viscosity considering the contributions of water slug, pressure drop due to interface shape of bubble and surface tension gradient. The calculated foam apparent viscosity was then introduced to modify the viscosity which governing the relationship between phase flow rates and pressure drop.

texture. Several studies further developed their models to consider the impacts of other elements such as the irregularly-shaped pores, wall roughness, etc. to consider a more actual condition. In this study, as the pores are assumed to be uniform and smooth, their foam apparent viscosity model is selected to represent methane−water slug rheological behavior. A more complicated and actual foam model to predict shale gas behavior will be considered in the following study.

In this case, the properties of near-surface water molecules are calculated according to liquid−solid molecular interactions analysis. This paper selects the empirical expression of $\mu_{\mathrm{wb}}(-0.018\theta+3.25)$ to calculate the near-surface water viscosity according to Wu et al. (2017), who relates the almost sticking water properties with pore wettability. Previous studies have used the

$$\frac{\mu_{\mathrm{f}}}{\mu_{\mathrm{wb}}}=L_{\mathrm{slug}}n_{\mathrm{f}}+0.85n_{\mathrm{f}}r\left/\left(\frac{r_{\mathrm{pl}}}{r}\right)\left(3\mu_{\mathrm{wb}}v_{\mathrm{g}}\left/\sigma\right)(3\mu_{\mathrm{wb}}v_{\mathrm{g}}/\sigma)^{-\frac{1}{3}}\left[1+\left(\frac{r_{\mathrm{pl}}}{r}\right)^{2}\right]+n_{\mathrm{f}}r\left(3\mu_{\mathrm{wb}}v_{\mathrm{g}}\left/(3\mu_{\mathrm{wb}}v_{\mathrm{g}}/\sigma)^{-\frac{1}{3}}\sqrt{N_{\mathrm{s}}}\tanh\left(L_{\mathrm{BD}}\left/2\right)\right.\right.\right.$$

$$(1)$$

where μ_{f} is the foam apparent viscosity, cP, which is used to represent the rheological property of water−gas bubble in water bridge model; μ_{wb} is the bulk water viscosity, cP; L_{slug} is the total water slug length, cm; n_{f} is the number of lamella per unit length, 1/m; r is the pore radius, m; r_{pl} is the radius of bubble plateau border, cm; v_{g} is the gas phase velocity, cm/s; σ is the water−gas interfacial tension, N/m; N_{s} and L_{BD} are dimensionless groups, which are related to the contribution of surface tension gradient. In this study, as the gas bubbles are different from the surfactant stabilized bubbles, only the contribution of liquid slug and the dynamic pressure drop of an isolated bubble are incorporated to mimic the flow resistance of water bridge for gas flow. The model proposed by Hirasaki and Lawson (1985) is the basis of the analytical pore-level modelling of foam behavior with foam

conclusions of Wu et al. (2017) in a similar way. For example, Zhang et al. (2017) used the empirical models of Wu et al. (2017) to calculate water slip length and the water viscosity near the nanopore wall to derive the model of apparent liquid permeability model in dual-wettability nanoporous media. In order to figure out liquid−liquid two-phase flow characteristics in hydrophilic nanochannels, Zhan et al. (2020) also used these models to calculate the slip boundary condition for water at the pore surface. Besides, Feng et al. (2018) used these models to calculate the water viscosity in interaction area for previously published models as a way to validate their model. In this study, the apparent viscosity of water−gas bubble flow area is calculated with Eq. (1) to introduce the influence of water bridge on shale gas flow. The remaining water molecules keep the bulk water properties.

2.2. Gas−water two phase flow model

Considering both water slippage and gas slippage at the solid nanoscale substrate and the liquid−gas contact area, Li et al. (2019) proposed an analytical model to describe the annular flow pattern and obtain the gas flow pattern in a wet condition (Eq. (2)).

properties of the low-mobility water layer remain unchanged as the water molecules in the vicinity of pore surface are not able to stay away from the solid molecular forces. Then foam viscosity μ_f is introduced according to Eq. (1) to account for the impacts of water bridge on gas transport. Therefore Eq. (2) is transformed as below:

$$
\begin{cases}
v_g = -\dfrac{\Delta P}{\mu_g L}\dfrac{\left(\dfrac{z_D h}{2}\right)^2}{2} + \dfrac{\Delta P}{\mu_g L}\left(\dfrac{h}{2}-h_{wh}-h_{wb}\right)\left[\dfrac{\left(\dfrac{h}{2}-h_{wh}-h_{wb}\right)}{2} + \dfrac{2-\sigma_{tma}}{\sigma_{tma}}\dfrac{\lambda}{1-a_{gs}\lambda}\right] \\
\quad + \dfrac{\Delta P}{2\mu_{wb}L}h_{wb}(h-2h_{wh}-h_{wb}) + \dfrac{\Delta P}{2\mu_{wh}L}\left(hh_{wh}+hl_{ws}-h_{wh}{}^2\right) \\
v_{wb} = -\dfrac{\Delta P}{\mu_{wb}L}\dfrac{\left(\dfrac{z_D h}{2}\right)^2}{2} + \dfrac{\Delta P}{\mu_{wb}L}\dfrac{\left(\dfrac{h}{2}-h_{wh}\right)^2}{2} + \dfrac{\Delta P}{2\mu_{wh}L}\left(hl_{ws}+hh_{wh}-h_{wh}{}^2\right) \\
v_{wh} = -\dfrac{\Delta P}{\mu_{wh}L}\dfrac{\left(\dfrac{z_D h}{2}\right)^2}{2} + l_{ws}\dfrac{\Delta P}{\mu_{wh}L}\dfrac{h}{2} + \dfrac{\Delta P}{\mu_{wh}L}\dfrac{h^2}{8}
\end{cases}
\tag{2}
$$

where z_D is the dimensionless location along the z axis, dimensionless; v stands for phase velocity, m/s; μ represents phase viscosity, Pa s; subscripts g, wb and wh refer to gas phase, bulk water and high-viscosity water respectively; ΔP is an applied pressure difference between the entrance and exit along the z axis, Pa; L measures the nanoscale capillary length along the x axis, m; h is the width of flow space along the z axis, m; L_{ws} is the water slip length, m, which depends on pore contact angle θ and is calculated empirically as $b_{ws}/(cos\theta+1)^2$ according to Wu et al. (2017); σ_{tma} is the tangential momentum accommodation coefficient, dimensionless; a_{gs} is the gas slip coefficient, dimensionless; λ defined as $\frac{\mu_g}{P}\sqrt{\frac{\pi ZRT}{2M_{gw}}}$, is the gas mean free path, m, which is highly related with gas molecular weight M_{gw}, reservoir temperature T and reservoir pressure P. Gas slippage is not considered and $\frac{2-\sigma_{tma}}{\sigma_{tma}}\frac{\lambda}{1-a_{gs}\lambda}$ is defined as zero initially in this study.

In this study, the derived gas flow mathematical model (Eq. (2)) is taken as the base model. Keeping the water saturation and pore size to be the same, the thickness of bubble flow area is the total thickness of bulk water layer and gas flow zone, which is calculated to be $(h - 2h_{wh})$. As previously assumed, both the thickness and
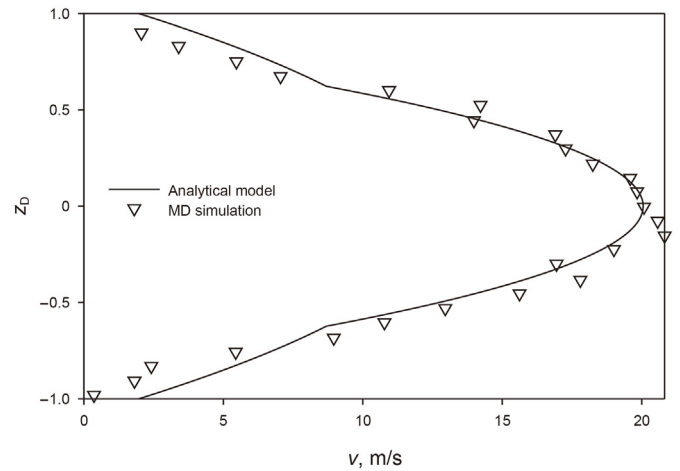
Fig. 2. Comparisons between the derived water bridge analytical model and MD simulation data (Ho and Striolo, 2015).

Table 1
Summary of modelling parameters (Ho and Striolo, 2015).

Parameter	Value	Parametr	Value
P	250 MPa	σ_{tma}	1
T	300 K	a_{gs}	-1
$\Delta P/L$	1.29×10^{15} Pa/m	L_{ws}	7.63×10^{-10} m
h	2.65×10^{-9} m	n_f	1.61×10^8
h_{wh}	0.5×10^{-9} m	r	1.33×10^{-9} m
μ_g	2.66×10^{-4} Pa s	r_{pl}	4.76×10^{-10} m
μ_{wb}	8.54×10^{-4} Pa s	σ	7.2×10^{-3} mN/m
μ_{wh}	2.30×10^{-3} Pa s	L	6.2×10^{-9} m

Table 2
Summary of modelling parameters.

Parameter	Value	Parameter	Value
P	250 MPa	μ_{wh}	2.7×10^{-3} Pa s
T	300 K	σ_{tma}	1
$\Delta P/L$	1.29×10^{15} Pa/m	a_{gs}	-1
h	2.65×10^{-9} m	S_w	0.7
h_{wh}	0.5×10^{-9} m	σ	7.2×10^{-3} mN/m
μ_g	2.66×10^{-4} Pa s	L	6.2×10^{-9} m
μ_{wb}	1.0×10^{-3} Pa s		
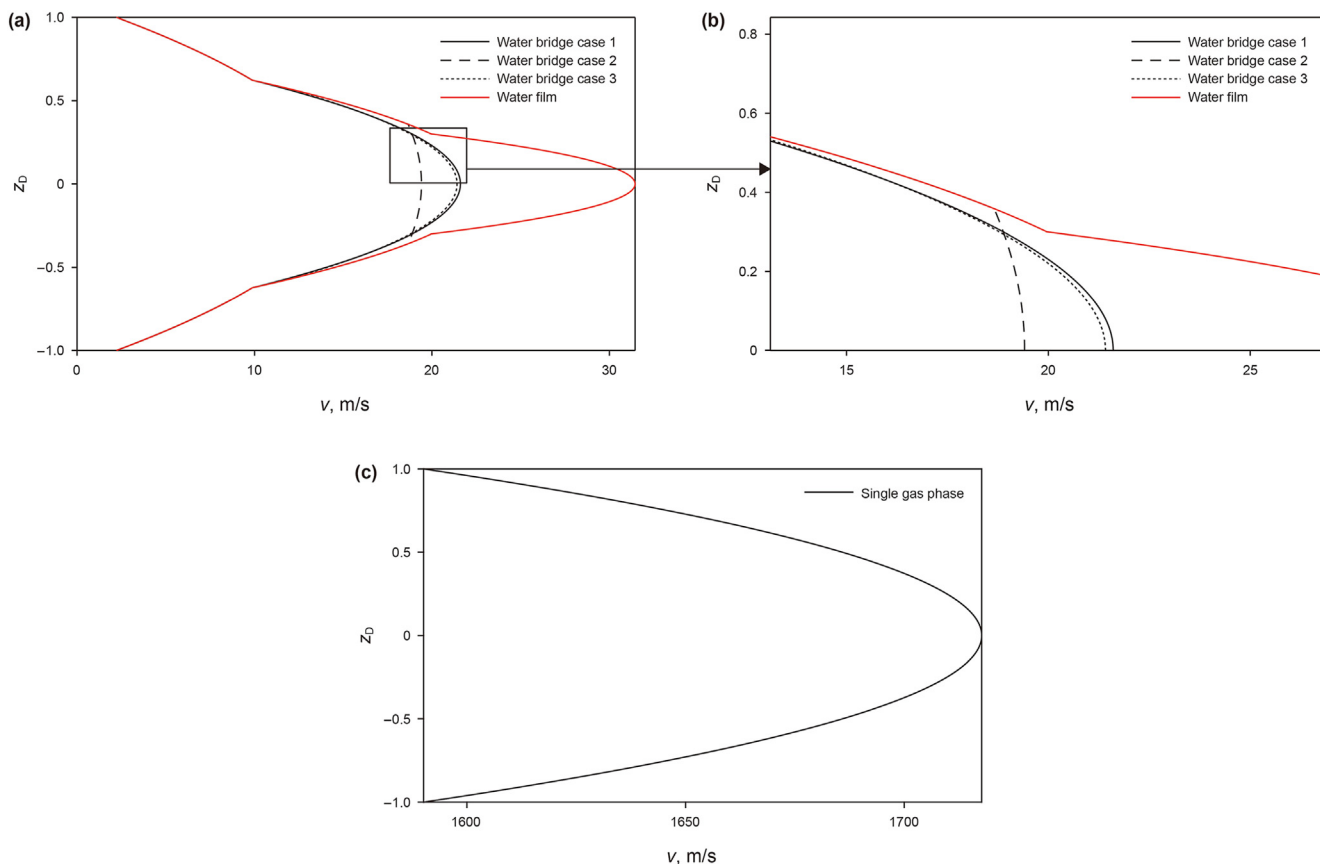
Fig. 3. (**a**) Velocity profiles of water bridge analytical model and bulk water analytical model (Li et al., 2019); (**b**) Comparison of part of velocity profiles between the derived water bridge analytical model and bulk water analytical model (Li et al., 2019); (**c**) Velocity profiles of single gas flow analytical model ($h = 2.65$ nm, $S_w = 0.7$, $T = 300$ K, $P = 250$ MPa, $h_{wh} = 0.5$ nm).

$$
\begin{cases}
v_f = -\dfrac{\Delta P}{\mu_f L}\dfrac{\left(\dfrac{z_D h}{2}\right)^2}{2} + \dfrac{\Delta P}{\mu_f L}\left(\dfrac{h}{2}-h_{wh}\right)\left[\dfrac{\left(\dfrac{h}{2}-h_{wh}\right)}{2}+\dfrac{2-\sigma_v}{\sigma_v}\dfrac{\lambda}{1-b\lambda}\right]+\dfrac{\Delta P}{2\mu_{wh}L}\left(hh_{wh}+hl_{ls}-h_{wh}{}^2\right) \\[3mm]
v_{wh} = -\dfrac{\Delta P}{\mu_{wh}L}\dfrac{z^2}{2}+l_{ls}\dfrac{\Delta P}{\mu_{wh}L}\dfrac{h}{2}+\dfrac{\Delta P}{\mu_{wh}L}\dfrac{h^2}{8}
\end{cases}
\tag{3}
$$

where v_f is the foam area velocity, m/s.

3. Model validation

The proposed model is validated with MD experiments data obtained by Ho and Striolo (2015). According to Ho and Striolo (2015), 1800 water molecules and 600 gas molecules are placed in the slit pore. The water bridge flow type is captured at the pressure of 250 MPa and when the acceleration is assigned 0.05 nm/ps^2. The pressure gradient along the pore length is calculated to be 1.29×10^{15} Pa/m according to Eq. (4) in this case. All the required validation parameters are listed in Table 1.

$$
\frac{\Delta P}{L} = -\frac{(N_g M_g + N_w M_w)}{N_A V}a
\tag{4}
$$

where N_g and N_w are the number of methane molecules and water molecules, dimensionless; M_g and M_w are the molar mass of methane and water, kg/mol; N_A is Avogadro constant, 6.02×10^{23} mol^{-1}; V is the pore volume, m^3; a is the acceleration, m/s^2.

Fig. 2 presents the validation result of the derived water bridge analytical model and the MD simulation data (Ho and Striolo, 2015) with the parameters listed in Table 1. The mean square error (MSE) indicating the relative difference between analytical results and MD experimental results is 1.456 m/s.

4. Results and discussion

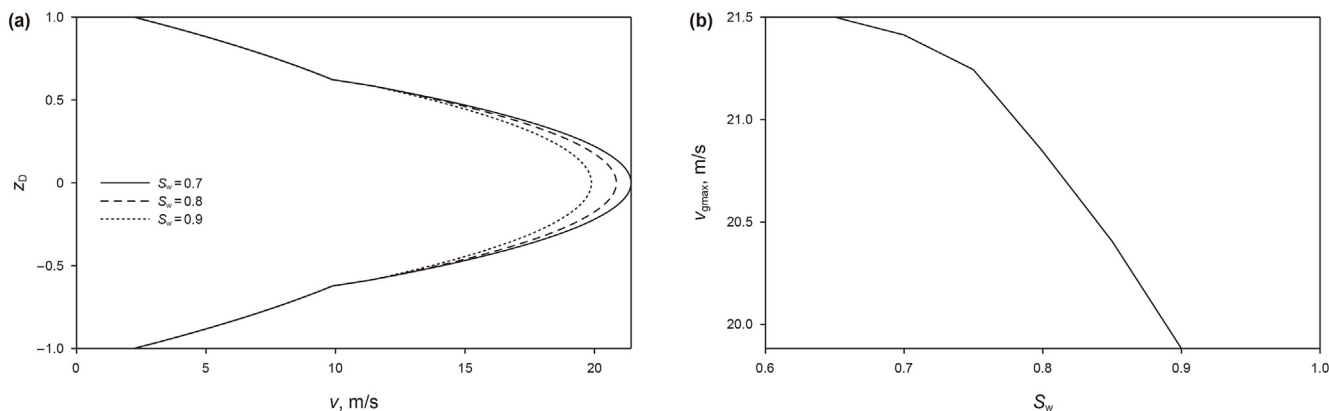Table 2 lists the modelling parameters for the results and discussion section.

Fig. 4. (**a**) Velocity profiles of water bridge analytical model when water saturation changes; (**b**) The relationship between water content with maximum gas flow rate ($h = 2.65$ nm, $T = 300$ K, $P = 250$ MPa, $h_{wh} = 0.5$ nm).

4.1. Velocity profiles comparisons

In Fig. 3a, water bridge case 1 refers to the extreme situation depicted in Fig. 1b when all bulk water molecules take the form of water bridge, resembling the liquid film of a methane bubble. In comparison, water bridge case 2 simulates the other extreme condition presented in Fig. 1c in which the liquid film of water bridge approaches the critical thickness and all the remaining bulk water molecules are reserved as a bulk water layer. Water bridge case 3 thus shows the velocity profile for the case in-between. Given the same acceleration, water content and channel dimension, the fluid velocity profile when water molecules are reserved as a bulk water film is also compared in Fig. 3a. To illustrate the impacts of water molecules, single gas flow velocity considering gas slippage is presented in Fig. 3c.

First of all, whether water molecules exist as a water bridge or not, the gas velocity profile takes the shape of a parabolic and the gas speed peak occurs at the centerline. Then, compared with the water bridge analytical model (case 3) accordingly, the gas molecules of water film analytical model have smaller flow area as the spread of bulk water layer takes a certain space. In Fig. 3a, the gas flow area of water film model takes the dimensionless area from -0.3 to 0.3 in the z axis while it occupies -0.5849 to 0.5849 for the water bridge model. However, without water molecules stay as a flowing barrier, the gas molecules of water film model move at a larger velocity which reaches 31.4491 m/s at the centerline. In comparison, the largest gas velocity is 21.4153 m/s when methane
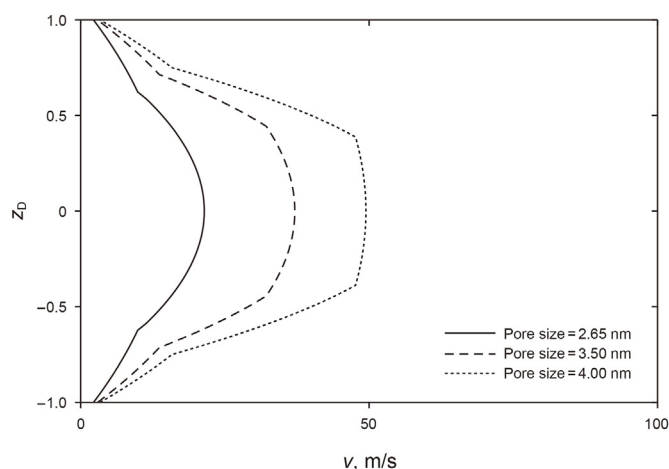

Fig. 6. Velocity profiles of water bridge analytical model when pore size changes ($S_w = 0.7$, $T = 300$ K, $P = 250$ MPa, $h_{wh} = 0.5$ nm).

bubble structure exists, 31.905% smaller than that of water film model. It confirms that the water bridge structure has a larger influence on gas flow capacity as water molecules spread across the whole gas flow section even though gas flow radius is less impacted.

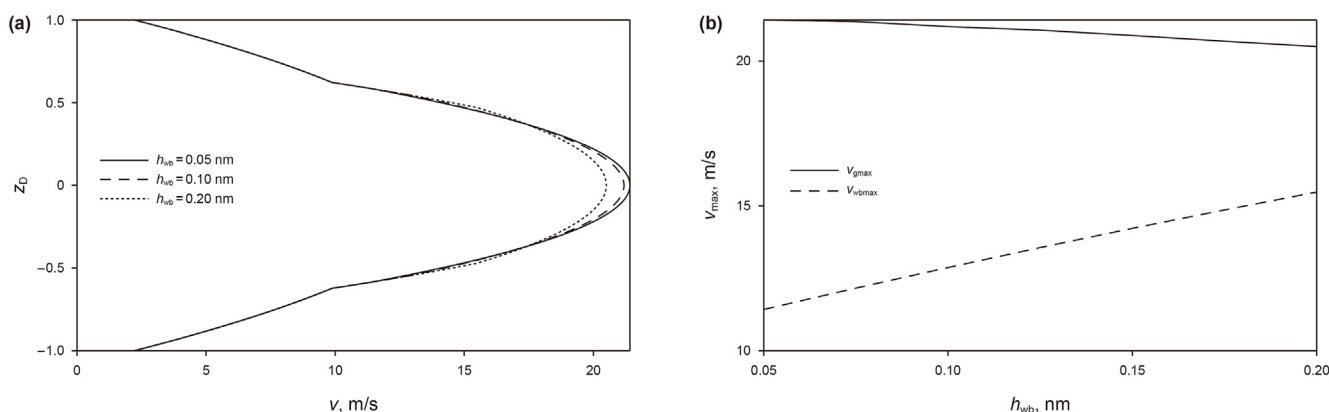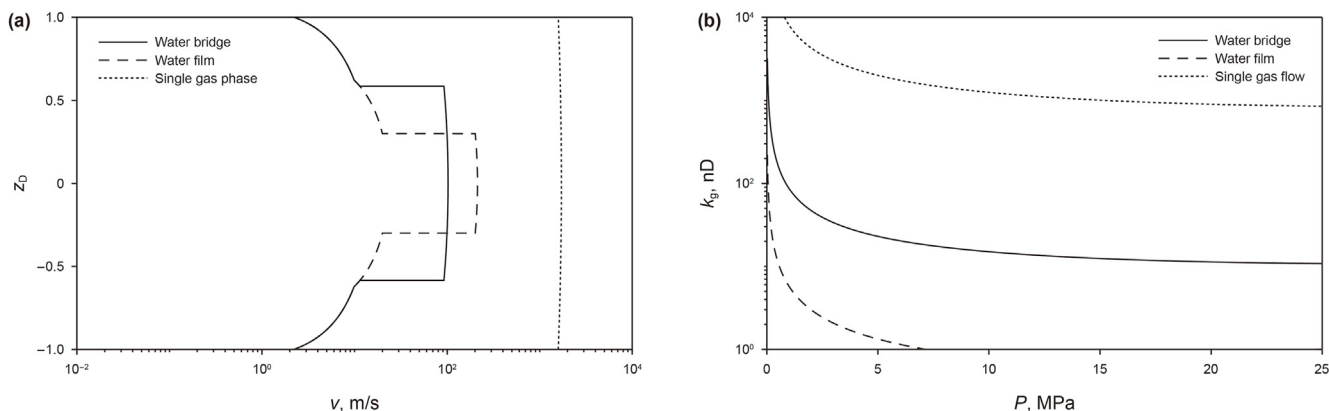Also, for the water bridge model (case 3) in Fig. 3b, it is apparent

Fig. 5. (**a**) Velocity profiles of water bridge analytical model when bulk water layer thickness changes; (**b**) The relationship between bulk water layer thickness with maximum gas flow rate and maximum bulk water rate ($h = 2.65$ nm, $S_w = 0.7$, $T = 300$ K, $P = 250$ MPa, $h_{wh} = 0.5$ nm).

Fig. 7. (**a**) Velocity profiles of water bridge analytical model, bulk water analytical model (Li et al., 2019) and single gas flow analytical model when considering gas slippage at water surface; (**b**) Gas apparent permeability of water bridge analytical model, bulk water analytical model (Li et al., 2019) and single gas flow analytical model when considering gas slippage at water surface ($h = 2.65$ nm, $S_w = 0.7$, $T = 300$ K, $h_{wh} = 0.5$ nm).

that the water molecules staying in the bulk water layer travel at the same speed as the bulk water molecules in water film model do. However, the water bridge molecules move at a smaller velocity as the foam apparent viscosity is larger than the bulk water viscosity.

The comparison between the three water bridge cases clarifies the importance of water bridge stability. With the same water saturation, the increase in water bridge thickness results in a smaller bubble viscosity and consequently a larger foam velocity. Obviously, a larger water bridge thickness brings about a smaller bulk water zone, extending the foam flow area. Furthermore, the increase in gas–water interface curvature of methane bubble, leading to a drop in the contribution from the interface deformed against the restoring force of surface tension caused by viscous and capillary forces, even though the contribution of liquid slug increases at this time. In consequence, the largest bubble velocity is 21.6067, 19.4130, and 21.4153 m/s, respectively, for the three cases in turn.

Fig. 3a, c explains the influence of water presence to gas flow qualitatively and quantitatively. Given a dry condition, gas molecules at the centerline are able to move at 1717.7 m/s with the help of gas slippage, which is much larger than the gas velocity in all the wet cases. For one thing, the existence of water film at the solid surface impedes gas–solid molecular interactions and reduces the gas slippage effect, and gas molecules consequently are not able to gain an extra velocity at the water–gas interface. For another thing, the gas flow space is occupied by the water molecules, which undermines gas transport ability to some extent.

4.2. Effect of water saturation

Fig. 4a analyzes the dependence of flow pattern on water saturation when the water bridge structure preserves. Maintaining bulk water layer thickness to be the same, an increase in water content signifies more water molecules accumulated in the water bridge, further leading to the increase in foam apparent viscosity as the increasing contribution of liquid slug outweighs the decreasing contribution from the interface deformation caused by viscous and capillary forces, which is consistence with the capillary suction theory declaring that a larger water saturation is conducive to preserve bubbles' stability and strength. Therefore, increasing water saturation from 0.7 to 0.8 and 0.9 results in the reduction of maximum gas flow velocity from 21.4153 to 20.8456 and 19.8835 m/s, respectively.

4.3. Effect of water bridge bulk film thickness

For the specified content of water molecules, increasing water bridge bulk film thickness simulates the collapse of water bridge when more and more water molecules leave water bridge to form bulk water film until the bridge thickness reaches the critical thickness. Comparing the three cases with different bulk water layer thickness in Fig. 5a comes with a conclusion that given the same water content, the reduction of bulk water layer thickness from 0.2 to 0.1 and 0.05 nm improves gas flow rate to varying degree. The maximum gas flow velocity increases from 20.5011 to 21.1848 and 21.4153 m/s, equaling to an increase by 3.335% and 4.459%. The reason goes to the smaller bubble viscosity caused by a larger gas–water interface curvature of methane bubble, which further reinforces the conclusion explaining the difference between two extreme conditions and a normal condition of water bridge structure in Fig. 3a. Also, as the pore size is specified, gas flow area stretch further facilitates gas transport in this case.

However, Fig. 5a is different from Fig. 4a as the bulk water layer thickness varies. A larger bulk water layer gives rise to a larger minimum gas flow rate (maximum bulk water rate) at the liquid–gas border. But its high viscosity reduces gas transport and achieves the smallest maximum gas flow rate at the centerline (Fig. 5b).

4.4. Effect of pore size

The three curves in Fig. 6 predict gas flow patterns with the same bubble radius in nanotubes measuring 2.65 to 3.50 and 4.00 nm separately. Keeping the almost sticking water film thickness to be 0.5 nm, the starting point for dimensionless high-viscosity water flow area changes from 0.6226, 0.7143 to 0.75 in turn. Simultaneously, the dimensionless flow range for gas phase turns out to be −0.5849 to 0.5849, −0.4429 to 0.4429, and −0.3875 to 0.3875 even though the absolute gas flow zone stays unchanged. In this case, increasing pore size from 2.65 to 3.50 and 4.00 nm brings about an increase in bulk water layer thickness from 0.05 to 0.475 and 0.725 nm, producing the methane bubble apparent viscosity of 1.16, 2.35, and 6.45 mPa s. However, a larger absolute bulk water flow area produces a larger overall flow capacity and therefore the maximum gas flow velocity turns out to be 21.4153, 37.1146, and 49.4475 m/s. The positive impact of a larger flow dimension overtakes the negative impact of a larger foam apparent viscosity. The contrast of the three curves with varying pore dimensions reveals that gas flow is more sensitive to water movement with a reduction in the pore size.

4.5. Gas slippage

The derived analytical model assumes that gas slippage disappears at the water–gas interface as water molecules act as a separator restricting gas–solid molecule collisions, which is consistent with the molecular dynamic simulation results of Liu et al. (2018). However, Sun et al. (2017) took gas slippage at water–gas interface into account during the derivation of an analytical model to predict gas apparent permeability in a wet condition, which was verified with various experimental and analytical results. Therefore, with the same parameters in Fig. 3a, Fig. 7a shows the flow profiles of water bridge, water film and single gas phase model supposing that gas slippage still exists at the water–gas interface.

It is obvious that gas slippage contributes significantly to gas flow capacity, resulting in the maximum gas velocity to be 102.2379 and 212.5433 m/s for water bridge model and water film model. Compared with the calculation results of Fig. 3a, gas slippage generates an increase in gas transport capacity by 4.774 times and 6.758 times, respectively.

Also, taking gas slippage into account makes gas apparent permeability during two phase flow to be highly dependent on reservoir pressure. For instance, gas apparent permeability turns out to be 10.7819, 0.5011, and 851.5771 nD separately for the three cases when the reservoir pressure equals 25 MPa as in Fig. 7b. It is estimated that reduction in effective gas flow space accounts for the drop of gas apparent permeability for the water film case.

Most previous investigations assumed that both water and gas were in form of annular flow in shale nanopores. For example, considering interfacial effects, Li et al. (2016b) attempted to obtain gas–water flow behavior in shale nanopores based on annular flow assumption. To derive gas–water relative permeability curves in hydrophilic nanopores, Zhang et al. (2017) assumed that water molecules distributed as water film on the wall and gas molecules flow in the central area. Likewise, with the assumption of uniform water films, Li et al. (2020) proposed an analytical model to calculate multiphase flow characteristics in fractal-like tree network. However, the two-phase flow is unsteady and annular flow does not exist throughout the production period. Therefore, this study puts forward another potential fluid flow pattern and estimate its impacts on shale gas flow behavior, which is conducive to a more comprehensive understanding of fluid flow and a more accurate prediction of gas production in share reservoirs.

5. Conclusions

Incorporating water slippage generated by water–solid molecular interactions and adopting foam apparent viscosity model to represent methane bubble rheological behavior, this paper derives an analytical model to illustrate the influences of water film and water slug on gas flow in shale nanopores. The following conclusions can be obtained:

(1) The impact of water bridge structure is larger than that of water film model on gas flow capacity as water molecules span the whole gas flow section even though they occupy a smaller gas flow area.

(2) Increasing water bridge thickness results in a smaller bubble viscosity and consequently a larger foam velocity given the same water content.

(3) Gas flow capacity is highest in a dry condition due to the contribution of gas slippage and a larger flow space. In this model, given a dry condition, the gas flow rate at the centerline is 85 times more than that in a wet condition when water saturation is 0.7.

(4) Maintaining bulk water layer thickness and increasing water bridge thickness tend to increase foam apparent viscosity and therefore undermine gas transport ability. In this model, reducing the bulk water layer thickness by 50% and 75% from 0.2 nm improves gas flow rate by 3.335% and 4.459%.

(5) The largest gas flow rate improves when more water molecules leave the bulk water zone as a result of a smaller bubble viscosity and a larger gas flow area.

(6) Gas transport ability is improved in larger nanopores even though there is a larger foam apparent viscosity when bulk water zone and gas zone are determined. For this model, the maximum gas flow velocity increases by 73.309% and 130.898% when the pore size increases from 2.65 to 3.50 and 4.00 nm.

(7) The consideration of gas slippage contributes to gas flow velocity both water film model and water bridge model. For this model, considering gas slippage generates an increase in gas transport capacity by 4.774 times and 6.758 times respectively.

References

Alcorn, Z.P., Føyen, T., Gauteplass, J., Benali, B., Soyke, A., Fernø, M., 2020. Pore-and core-scale insights of nanoparticle-stabilized foam for CO_2-enhanced oil recovery. Nanomaterials 10 (10), 1917. https://doi.org/10.3390/nano10101917.

Alharthy, N.S., Teklu, T.W.W., Nguyen, T.N., Kazemi, H., Graves, R.M., 2016. Nanopore compositional modeling in unconventional shale reservoirs. SPE Reservoir Eval. Eng. 19 (3), 415–428. https://doi.org/10.2118/166306-PA.

Cristancho-Albarracin, D., Akkutlu, I.Y., Criscenti, L.J., Wang, Y., 2017. Shale gas storage in kerogen nanopores with surface heterogeneities. Appl. Geochem. 84, 1–10. https://doi.org/10.1016/j.apgeochem.2017.04.012.

Feng, D., Li, X., Wang, X., Li, J., Zhang, X., 2018. Capillary filling under nano-confinement: the relationship between effective viscosity and water-wall interactions. Int. J. Heat Mass Tran. 118, 900–910. https://doi.org/10.1016/j.ijheatmasstransfer.2017.11.049.

Fu, C., Liu, N., 2020. Study of the synergistic effect of the nanoparticle-surfactant-polymer system on CO_2 foam apparent viscosity and stability at high pressure and temperature. Energy Fuels 34 (11), 13707–13716. https://doi.org/10.1021/acs.energyfuels.0c02435.

Garum, M., Glover, P.P., Hassanpour, A., Lorinczi, P.P., 2019. Fluid flow and micro-structural properties of gas shales. In: 81st EAGE Conference and Exhibition 2019. European Association of Geoscientists & Engineers. https://doi.org/10.3997/2214-4609.201901110.

Guo, C., Liu, H., Xu, L., Zhou, Q., 2019. An improved transport model of shale gas considering three-phase adsorption mechanism in nanopores. J. Pet. Sci. Eng. 182, 106291. https://doi.org/10.1016/j.petrol.2019.106291.

Gupta, N., Fathi, E., Belyadi, F., 2018. Effects of nano-pore wall confinements on rarefied gas dynamics in organic rich shale reservoirs. Fuel 220, 120–129. https://doi.org/10.1016/j.fuel.2018.01.120.

Hatami, M., Bayless, D., Sarvestani, A., 2020. A model for stress-dependence of apparent permeability in nanopores of shale gas reservoirs. AIChE J. 66 (10), e16541. https://doi.org/10.1002/aic.16541.

Herdes, C., Petit, C., Mejía, A., Müller, E.A., 2018. Combined experimental, theoretical, and molecular simulation approach for the description of the fluid-phase behavior of hydrocarbon mixtures within shale rocks. Energy Fuels 32 (5), 5750–5762. https://doi.org/10.1021/acs.energyfuels.8b00200.

Hirasaki, G.J., Lawson, J.B., 1985. Mechanisms of foam flow in porous media: apparent viscosity in smooth capillaries. SPE J. 25 (2), 176–190. https://doi.org/10.2118/12129-PA.

Ho, T.A., Striolo, A., 2015. Water and methane in shale rocks: flow pattern effects on fluid transport and pore structure. AIChE J. 61, 2993–2999. https://doi.org/10.1002/aic.14869.

Ho, T.A., Wang, Y., 2020. Pore size effect on selective gas transport in shale nano-pores. J. Nat. Gas Sci. Eng. 83, 103543. https://doi.org/10.1016/j.jngse.2020.103543.

Hou, P., Gao, F., He, J., Liu, J., Xue, Y., Zhang, Z., 2020. Shale gas transport mechanisms

in inorganic and organic pores based on lattice Boltzmann simulation. Energy Rep. 6, 2641–2650.

Islam, A.W., Sun, A.Y., 2017. A theory-based simple extension of Peng–Robinson equation of state for nanopore confined fluids. J. Pet. Explor. Prod. Technol. 7 (4), 1197–1203. https://doi.org/10.1016/j.egyr.2020.09.021.

Jia, B., Tsau, J.S., Barati, R., 2020. Investigation of shale-gas-production behavior: evaluation of the effects of multiple physics on the matrix. SPE Reservoir Eval. Eng. 23 (1), 68–80.

Jin, Z., Firoozabadi, A., 2015. Flow of methane in shale nanopores at low and high pressure by molecular dynamics simulations. J. Chem. Phys. 143 (10), 104315. https://doi.org/10.2118/197069-PA.

Kibria, M.G., Hu, Q., Liu, H., Zhang, Y., Kang, J., 2018. Pore structure, wettability, and spontaneous imbibition of Woodford shale, Permian Basin, West Texas. Mar. Petrol. Geol. 91, 735–748. https://doi.org/10.1016/j.marpetgeo.2018.02.001.

Li, J., Li, X., Wu, K., Wang, X., Shi, J., Yang, L., Zhang, H., Sun, Z., Wang, R., Feng, D., 2016a. Water sorption and distribution characteristics in clay and shale: effect of surface force. Energy Fuels 30 (11), 8863–8874. https://doi.org/10.1021/acs.energyfuels.6b00927.

Li, J., Li, X., Wu, K., Feng, D., Zhang, T., Zhang, Y., 2017. Thickness and stability of water film confined inside nanoslits and nanocapillaries of shale and clay. Int. J. Coal Geol. 179, 253–268. https://doi.org/10.1016/j.coal.2017.06.008.

Li, R., Wu, K., Li, J., Xu, J., Chen, Z., 2019. Shale gas transport in wedged nanopores with water films. J. Nat. Gas Sci. Eng. 66, 217–232. https://doi.org/10.1016/j.jngse.2019.04.001.

Li, R., Chen, Z., Wu, K., Liu, X., Dou, L., Yang, S., Xu, J., 2020. A fractal model for gas-water relative permeability curve in shale rocks. J. Nat. Gas Sci. Eng. 81, 103417. https://doi.org/10.1016/j.jngse.2020.103417.

Li, T., Song, H., Wang, J., Wang, Y., Killough, J., 2016b. An analytical method for modeling and analysis gas-water relative permeability in nanoscale pores with interfacial effects. Int. J. Coal Geol. 159, 71–81. https://doi.org/10.1016/j.coal.2016.03.018.

Liu, B., Qi, C., Zhao, X., Teng, G., Zhao, L., Zheng, H., Zhan, K., Shi, J., 2018. Nanoscale two-phase flow of methane and water in shale inorganic matrix. J. Phys. Chem. C 122 (46), 26671–26679. https://doi.org/10.1021/acs.jpcc.8b06780.

Mistré, M., Crénes, M., Hafner, M., 2018. Shale gas production costs: historical developments and outlook. Energy Strategy Rev. 20, 20–25. https://doi.org/10.1016/j.esr.2018.01.001.

Rubin, C., Zamirian, M., Takbiri-Borujeni, A., Gu, M., 2019. Investigation of gas slippage effect and matrix compaction effect on shale gas production evaluation and hydraulic fracturing design based on experiment and reservoir simulation. Fuel 241, 12–24. https://doi.org/10.1016/j.fuel.2018.12.015.

Song, W., Yao, J., Wang, D., Li, Y., Sun, H., Yang, Y., 2020a. Dynamic pore network modelling of real gas transport in shale nanopore structure. J. Nat. Gas Sci. Eng. 184, 106506. https://doi.org/10.1016/j.petrol.2019.106506.

Song, Z., Song, Y., Guo, J., Zhang, Z., Hou, J., 2020b. Adsorption induced critical shifts of confined fluids in shale nanopores. Chem. Eng. J. 385, 123837. https://doi.org/10.1016/j.cej.2019.123837.

Sun, Z., Li, X., Shi, J., Zhang, T., Sun, F., 2017. Apparent permeability model for real gas transport through shale gas reservoirs considering water distribution characteristic. Int. J. Heat Mass Tran. 115, 1008–1019. https://doi.org/10.1016/j.ijheatmasstransfer.2017.07.123.

Sun, Z., Shi, J., Wu, K., Zhang, T., Feng, D., Huang, L., Shi, Y., Ramachandran, H., Li, X., 2019. An analytical model for gas transport through elliptical nanopores. Chem. Eng. Sci. 199, 199–209. https://doi.org/10.1016/j.ces.2019.01.013.

Swami, V., Clarkson, C.R., Settari, A., 2012. Non-Darcy flow in shale nanopores: do we have a final answer?. In: SPE Canadian Unconventional Resources Conference. Society of Petroleum Engineers. https://doi.org/10.2118/162665-MS.

Tesson, S., Firoozabadi, A., 2018. Methane adsorption and self-diffusion in shale kerogen and slit nanopores by molecular simulations. J. Phys. Chem. C 122 (41), 23528–23542. https://doi.org/10.1021/acs.jpcc.8b07123.

Wan, T., Mu, Z., 2018. The use of numerical simulation to investigate the enhanced Eagle Ford shale gas condensate well recovery using cyclic CO₂ injection method with nano-pore effect. Fuel 233, 123–132. https://doi.org/10.1016/j.fuel.2018.06.037.

Wang, H., Chen, L., Qu, Z., Yin, Y., Kang, Q., Yu, B., Tao, W.Q., 2020. Modeling of multi-scale transport phenomena in shale gas production—a critical review. Appl. Energy 262, 114575. https://doi.org/10.1016/j.apenergy.2020.114575.

Wang, S., Feng, Q., Zha, M., Javadpour, F., Hu, Q., 2018. Supercritical methane diffusion in shale nanopores: effects of pressure, mineral types, and moisture content. Energy Fuels 32 (1), 169–180. https://doi.org/10.1021/acs.energyfuels.7b02892.

Wang, S., Feng, Q., Javadpour, F., Hu, Q., Wu, K., 2019. Competitive adsorption of methane and ethane in montmorillonite nanopores of shale at supercritical conditions: a grand canonical Monte Carlo simulation study. Chem. Eng. J. 355, 76–90. https://doi.org/10.1016/j.cej.2018.08.067.

Wu, K., Chen, Z., Li, J., Li, X., Xu, J., Dong, X., 2017. Wettability effect on nanoconfined water flow. Proc. Natl. Acad. Sci. USA 114, 3358–3363. https://doi.org/10.1073/pnas.1612608114.

Wu, Q., Ok, J.T., Sun, Y., Retterer, S.T., Neeves, K.B., Yin, X., Bai, B., Ma, Y., 2013. Optic imaging of single and two-phase pressure-driven flows in nano-scale channels. Lab Chip 13 (6), 1165–1171. https://doi.org/10.1039/C2LC41259D.

Xiong, J., Liu, X., Liang, L., Zeng, Q., 2017. Adsorption of methane in organic-rich shale nanopores: an experimental and molecular simulation study. Fuel 200, 299–315. https://doi.org/10.1016/j.fuel.2017.03.083.

Xu, H., Yu, H., Fan, J., Zhu, Y., Wang, F., Wu, H., 2020. Two-phase transport characteristic of shale gas and water through hydrophilic and hydrophobic nanopores. Energy Fuels 34 (4), 4407–4420. https://doi.org/10.1021/acs.energyfuels.0c00212.

Xu, J., Wu, K., Yang, S., Cao, J., Chen, Z., 2017. Nanoscale free gas transport in shale rocks: a hard-sphere based model. In: SPE Unconventional Resources Conference. OnePetro. https://doi.org/10.2118/185022-MS.

Xu, J., Wu, K., Li, R., Li, Z., Li, J., Xu, Q., Chen, Z., 2018a. Real gas transport in shale matrix with fractal structures. Fuel 219, 353–363. https://doi.org/10.1016/j.fuel.2018.01.114.

Xu, J., Wu, K., Li, Z., Pan, Y., Li, R., Li, J., Chen, Z., 2018b. A model for gas transport in dual-porosity shale rocks with fractal structures. Ind. Eng. Chem. Res. 57 (18), 6530–6537. https://doi.org/10.1021/acs.iecr.8b00021.

Xu, J., Wu, K., Li, R., Li, Z., Li, J., Xu, Q., Li, L., Chen, Z., 2019a. Nanoscale pore size distribution effects on gas production from fractal shale rocks. Fractals 27 (8), 1950142. https://doi.org/10.1142/S0218348X19501421.

Xu, R., Prodanović, M., Landry, C.J., 2019b. Study of subcritical and supercritical gas adsorption behavior in different nanopore systems in shale using lattice Boltzmann method. Int. J. Coal Geol. 212, 103263. https://doi.org/10.1016/j.coal.2019.103263.

Yassin, M.R., Begum, M., Dehghanpour, H., 2017. Organic shale wettability and its relationship to other petrophysical properties: a Duvernay case study. Int. J. Coal Geol. 169, 74–91. https://doi.org/10.1016/j.coal.2016.11.015.

Yekeen, N., Padmanabhan, E., Idris, A.K., 2018. A review of recent advances in foam-based fracturing fluid application in unconventional reservoirs. J. Ind. Eng. Chem. 66, 45–71. https://doi.org/10.1016/j.jiec.2018.05.039.

Yin, Y., Qu, Z.G., Zhang, J.F., 2017. An analytical model for shale gas transport in kerogen nanopores coupled with real gas effect and surface diffusion. Fuel 210, 569–577. https://doi.org/10.1016/j.fuel.2017.09.018.

Zeng, Y., Ning, Z., Wang, Q., Sun, H., Huang, L., Ye, H., 2018. Gas transport in self-affine rough microchannels of shale gas reservoir. J. Petrol. Sci. Eng. 167, 716–728. https://doi.org/10.1016/j.petrol.2018.04.045.

Zhan, S., Su, Y., Jin, Z., Zhang, M., Wang, W., Hao, Y., Li, L., 2020. Study of liquid-liquid two-phase flow in hydrophilic nanochannels by molecular simulations and theoretical modeling. Chem. Eng. Sci. 395, 125053. https://doi.org/10.1016/j.cej.2020.125053.

Zhang, T., Li, X., Sun, Z., Feng, D., Miao, Y., Li, P., Zhang, Z., 2017. An analytical model for relative permeability in water-wet nanoporous media. Chem. Eng. Sci. 174, 1–12. https://doi.org/10.1016/j.ces.2017.08.023.

Zuo, J.Y., Guo, X., Liu, Y., Pan, S., Canas, J., Mullins, O.C., 2018. Impact of capillary pressure and nanopore confinement on phase behaviors of shale gas and oil. Energy Fuels 32 (4), 4705–4714. https://doi.org/10.1021/acs.energyfuels.7b03975.